

# Switched amplifier-driven nanopositioning: Integrating system modeling and control tuning

Daniel Pechgraber, Johannes Wiesböck, Ernst Csencsics, and Georg Schitter

**Abstract**—This paper presents the integrated mechatronic and control design of a switched current amplifier-driven high-precision positioning system. An optimization based parameter tuning process for a highly integrated state-control structure is proposed, including both dynamic requirements and target positioning uncertainty. This is enabled by a dynamic error budgeting analysis in the frequency domain, which is used to estimate position error contributions of the dominant error sources in the control system. The theoretical results are validated in practical experiments on a built prototype system, revealing a steady-state positioning uncertainty of 0.6nm (rms) and fast reference position tracking with a rise-time of 0.64ms. Additionally 17% less overshoot in comparison to classical loop-shaping cascade-controllers is demonstrated.

**Index Terms**—Nanometer positioning, Switched amplifier, Precision, Controller tuning, Dynamic error budgeting

## I. INTRODUCTION

HIGH-precision motion systems can be found in various applications throughout the high-tech industry, like semiconductor manufacturing [1], atomic-force microscopy [2], and 3D-printing [3]. Many of these systems rely on electromagnetic Lorentz-force actuation because of its favorable properties, such as the linear relation between force and current or (quasi) zero-stiffness [4], [5]. Zero-stiffness implies that vibrations originating from the stator are naturally isolated from the moving part of the actuator due to a position independent force, which makes them well suited for high-precision applications on the nano-scale [6]. The moving part is usually constrained in the not actuated degrees of freedom by either magnetic levitation [7] or air bearings [8], to keep the zero-stiffness property, or by mechanical flexure structures [6], [9]. The latter, often the simplest and cheapest solution, can still transmit vibrations from the stator to the mover via the non-zero flexure stiffness, which is typically counteracted by a high-bandwidth position control loop [10].

Manuscript received Month 2xxx; revised Month xx, 2xxx; accepted Month xx, 2xxxx. The partly financial support by the Austrian Federal Ministry of Labour and Economy, the National Foundation for Research, Technology and Development and the Christian Doppler Research Association, and Micro-Epsilon Atensor GmbH and MICRO-EPSILON-MESSTECHNIK GmbH & Co.K.G. is gratefully acknowledged.

The authors are with the Advanced Mechatronic Systems (AMS) group at the Automation and Control Institute (ACIN), TU Wien, 1040 Vienna, Austria (e-mail: pechgraber@acin.tuwien.ac.at).

Daniel Pechgraber and Ernst Csencsics are with the Christian Doppler Laboratory for Precision Measurements in Motion, Automation and Control Institute (ACIN), TU Wien, 1040 Vienna, Austria.

The high-precision position control loops for Lorentz-force actuated positioning systems are usually implemented as cascaded control-structure incorporating an inner current control loop with a current amplifier and an outer position control loop [11]. Switched current amplifiers offer advantages over classical linear amplifiers due to their enhanced energy efficiency and minimized heat generation [11]. This is particularly important in precision positioning applications within limited-space environments, where thermal expansion effects can be a significant concern. On the other hand they introduce additional current ripple and the need for more complex modulation schemes and current measurement procedures as compared to linear current amplifiers and are therefore often avoided [12], [13].

There are many publications focusing on the development of high-precision current amplifiers alone, without taking into account their effect on the precision in a position control-loop. A combination of a Luenberger estimator, an Linear Quadratic Regulator (LQR) for fast transient response and an outer frequency domain controller is used for controlling a high-precision industrial current amplifier [14]. A more general approach studies the contribution of the current amplifier to the overall system precision by analysing the error propagation through the entire mechatronic system including the outer position control loop [15]. It takes into account offset errors, gain errors and non-linearity errors of the amplifier and the bandwidth of the current control loop. This investigation is further extended to current measurement noise and spurious signals occurring in the current amplifier in [16].

Especially measurement noise coupled into the system by closing the current-control loop is considered a major cause for current amplifier related positioning uncertainties [17]. A common approach to reduce the effects of measurement noise in a control system is the implementation of a Kalman-filter as state-observer, which takes two parameters, the measurement noise covariance and the process noise covariance of the system. These parameters are widely depending on the problem and measurement system and there is no commonly accepted method to tune the filter properly [18]. Mostly it is tuned by trial-and error, or an optimization process based on real measured data is used to minimize certain performance metrics, like the normalized estimation error squared (NEES) [19], [20]. However, the primary focus of precision positioning systems is the positioning uncertainty at the output, which is not directly used in the tuning of the controller parameters so far.

The contribution of this paper is the integrated design of

a switched amplifier-driven nanopositioning system and the systematic tuning of a state-control structure, based on a dynamic error budget analysis in the frequency domain.

## II. SYSTEM DESCRIPTION AND MODELLING

The system under investigation is a 1 degree of freedom (DoF) motion system actuated by a Lorentz actuator which is driven by a switched current amplifier. In this section the principle structure of the system is introduced and a comprehensive mathematical model is derived, considering the electrical as well as the magnetical and mechanical system together with their dynamic coupling.

### A. Switched amplifier based 1 DoF positioning system

The mechanical system comprises a mover, which is suspended by a mechanical flexure structure which constrains the 5 non-actuated DoFs. The mover is rigidly connected to the moving part of a voice coil actuator (VCA), serving as the positioning mechanism. To enable high accelerations, the mover mass is kept as low as possible. This also showcases the achievable precision with the proposed control structure, because lighter masses are inherently more responsive to external disturbance forces and it is therefore more challenging to minimize the position uncertainty. Fig. 1 shows the principle mechanical structure together with the circuit diagram of a switched current amplifier for driving the Lorentz actuator [14].

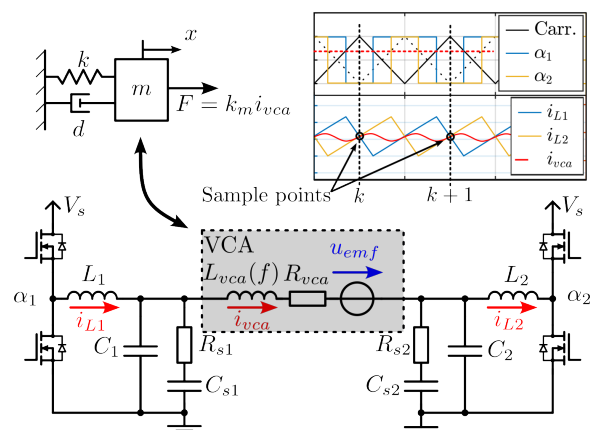


Fig. 1. Circuit diagram of switched current amplifier together with its connection to the VCA and the mechanical system represented as a mass-spring-damper system. Due to the symmetric on-times of both half-bridges around the center-aligned carrier signal, the mean-value of the actuator current can be extracted without the need for additional filtering.

The amplifier has a full-bridge topology including 4 MOSFETs, switched corresponding to the respective duty-cycle values  $\alpha_1$  and  $\alpha_2$ . This topology has the advantage, that only one supply rail  $V_s$  is necessary for driving the VCA voltage in the range from  $-V_s$  to  $+V_s$ . A small dead-time between the switching transitions ensures, that no short-circuit occurs on either side. A center-aligned triangular carrier waveform

is used for the PWM-generation on each side as sketched in Fig. 1, leading to a symmetric on-time of each half-bridge around the center of the carrier signal. Due to this symmetry, the mean-value of the actuator current  $i_{vca}$ , which is used for the control, can directly be extracted by sampling the current in the center of the triangular carrier. This eliminates the need for filtering the superimposed current ripple, which would introduce unacceptable delays in the control loop. A further advantage is, that at these time instants ( $k, k+1, \dots$ ) switching events in the MOSFETs only occur in the extreme duty-cycle cases  $\alpha = 0$  or  $\alpha = 1$ , which can be avoided by design. This improves the robustness of the current measurement against electrical disturbances arising from the MOSFET switching. To reduce current ripple and EMI, an LC output filter is integrated on either half-bridge side, which makes it a viable solution for EMI-sensitive environments.

### B. Mathematical modelling

In order to derive the mathematical model for the entire electro-mechanical system, at first the electronic circuit from Fig. 1 has to be investigated in more detail. The VCA consists of the inductance  $L_{vca}(f)$ , its copper resistance  $R_{vca}$  and the back-induced voltage  $u_{emf}$  originating from the movement of the VCA. Measurements show a distinct frequency dependency of the inductance, which can be explained by an eddy-current induced magnetic flux in the stator parts of the VCA opposing the flux generated by the actuator current. The LC-output filter on both sides ( $L_1, C_1, L_2, C_2$ ) reduces the current ripple in the VCA resulting from the PWM-switching. For damping the resonance peak of the LC-output filter, additional RC-snubber circuits are added ( $R_{s1}, C_{s1}, R_{s2}, C_{s2}$ ).

Under the assumption of symmetric component values on both sides ( $L_1 = L_2, C_1 = C_2, \dots$ ) and with the reduction of the two duty-cycle inputs to one generalized duty-cycle input  $\alpha$  with  $\alpha_1 = \alpha$ , and  $\alpha_2 = 1 - \alpha$  the full-bridge topology of Fig. 1 can be equivalently expressed by a state-space averaged (time-average over one PWM switching period) one-sided circuit model as depicted in Fig. 2 [21]. The equivalent component

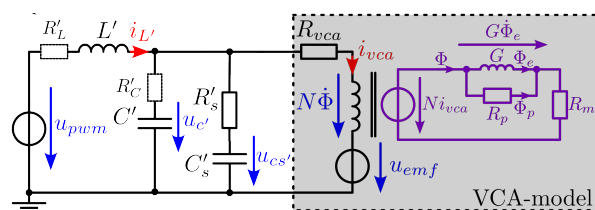


Fig. 2. Equivalent amplifier model for symmetric component values and one generalized duty-cycle input  $\alpha$ . The frequency dependency of the VCA inductance is modelled in the magnetic domain with the main reluctance  $R_m$ , the magnetic equivalent of an inductance  $G$  representing eddy-currents, and a parallel reluctance  $R_p$ .

values for the output filter and the snubber-circuit are then calculated by  $L' = 2L_1, C' = C_1/2, R'_s = R_{s1}$  and  $C'_s = C_{s1}/2$ . With  $R'_L$  and  $R'_C$  additionally the parasitic resistances of  $L'$  and  $C'$  are considered. The state-space averaged input

voltage  $u_{pwm}$  ranges from the negative supply voltage  $-V_s$  to the positive supply voltage  $V_s$  and is calculated by

$$u_{pwm} = (2\alpha - 1) V_s, \alpha \in [0, 1]. \quad (1)$$

As shown in the grey box of Fig. 2, the VCA representation is refined to model the frequency dependency of the inductance  $L_{vca}$  originating from eddy-current effects. Therefore the system is split into two Kirchhoffian domains, one magnetic and one electric [22]. In the magnetic domain eddy-currents are represented by a "magnetic inductance"  $G$ , which counteracts the magnetic flux generated by the current  $i_{vca}$  together with a parasitic parallel reluctance  $R_p$ . At zero frequency the "magnetic inductance"  $G$  has no effect and the actuator inductance is determined with the coil windings  $N$  and the main reluctance  $R_m$  by the well-known formula  $L_{vca}(0) = \frac{N^2}{R_m}$ .  $\Phi_e$  represents the magnetic flux through the eddy-current inductance and  $\Phi_p$  the flux through the parasitic reluctance  $R_p$ . With  $\Phi = \Phi_e + \Phi_p$ , the coupling between the electrical and magnetical domain is given by

$$N i_{vca} = G \dot{\Phi}_e + R_m \Phi, \quad (2a)$$

$$u_{vca} = R_{vca} i_{vca} + N \dot{\Phi} + u_{emf}, \quad (2b)$$

$$\Phi_p = \frac{G \dot{\Phi}_e}{R_p}. \quad (2c)$$

It is to note, that the magnetical parameters ( $N$ ,  $G$ ,  $R_m$ ,  $R_p$ ) can not be directly obtained from Fig. 1, so they are determined later in the system identification process (Section V-A). Further the actuator resistance  $R_{vca}$  is subject to heating in the copper windings, which leads to a change in resistance [23]. However, as thermal effects are slow compared to the target control bandwidth, the inclusion of an integrator will cope with these changes instead of explicitly modeling it.

The mechanical subsystem of the positioning system is modeled as mass-spring-damper system with the mover mass  $m$ , spring constant  $k$  and damping coefficient  $d$  (see Fig. 1). It is dynamically coupled to the electrical subsystem by the actuator force  $F$  and the counter induced voltage  $u_{emf}$ . The coupling equations between magnetical and mechanical subsystem are

$$F = k_m i_{vca}, \quad (3a)$$

$$u_{emf} = k_m \dot{x}, \quad (3b)$$

with the actuator motor constant  $k_m$  and mover velocity  $\dot{x}$ . For simplicity it is assumed that the actuator motor constant  $k_m$  is independent from the mover position  $x$ , which is valid for small motion ranges [4]. To control the position, measurements of both actuator current  $i_{vca}$  and the mover position  $x$  are accessible.

With the states  $\mathbf{x} = [\dot{x} \ x \ i_{L'} \ u_{c'} \ u_{cs'} \ \dot{\Phi}_e \ \Phi_e]^T$ , the input  $u = u_{pwm}$ , the output  $\mathbf{y} = [x \ i_{vca}]^T$ ,  $\mathbf{A} \in \mathbb{R}^{7 \times 7}$ ,  $\mathbf{b} \in \mathbb{R}^{7 \times 1}$  and  $\mathbf{C} \in \mathbb{R}^{2 \times 7}$ , the continuous dynamic model of the entire

mechatronic system can be derived in the state-space form

$$\dot{\mathbf{x}} = \underbrace{\begin{bmatrix} \mathbf{A}_{11} & \mathbf{0} & \mathbf{A}_{13} \\ \mathbf{0} & \mathbf{A}_{22} & \mathbf{A}_{23} \\ \mathbf{A}_{31} & \mathbf{A}_{32} & \mathbf{A}_{33} \end{bmatrix}}_{\mathbf{A}} \mathbf{x} + \underbrace{\begin{bmatrix} 0 & 0 & \frac{1}{L'} & 0 & 0 & 0 & 0 \end{bmatrix}^T}_{\mathbf{b}^T} u, \quad (4a)$$

$$\mathbf{y} = \underbrace{\begin{bmatrix} 0 & 1 & 0 & 0 & 0 & 0 & 0 \\ 0 & 0 & 0 & 0 & 0 & \frac{G(R_m + R_p)}{NR_p} & \frac{R_m}{N} \end{bmatrix}}_{\mathbf{C}} \mathbf{x}. \quad (4b)$$

The dynamic matrix  $\mathbf{A}$  is partitioned into the mechanical part

$$\mathbf{A}_{11} = \begin{bmatrix} -\frac{d}{m} & -\frac{k}{m} \\ 1 & 0 \end{bmatrix}, \quad (5)$$

the electrical part

$$\mathbf{A}_{22} = \begin{bmatrix} \frac{(-R'_s - R'_l)R'_C - R'_s R'_L}{L'(R'_C + R'_s)} & \frac{-R'_s}{(R'_C + R'_s)L'} & \frac{-R'_C}{(R'_C + R'_s)L'} \\ \frac{R'_L}{C'(R'_C + R'_s)} & \frac{-1}{C'(R'_C + R'_s)} & \frac{1}{C'(R'_C + R'_s)} \\ \frac{R'_C}{C'_s(R'_C + R'_s)} & \frac{1}{C'_s(R'_C + R'_s)} & \frac{-1}{C'_s(R'_C + R'_s)} \end{bmatrix}, \quad (6)$$

and the magnetical part

$$\mathbf{A}_{33} = \begin{bmatrix} a_1 & a_2 \\ 1 & 0 \end{bmatrix}, \quad (7)$$

with

$$a_1 = \frac{-((R_{vca} + R'_s)R'_C + R_{vca}R'_s)(R_m + R_p)}{N^2(R'_C + R'_s)} - \frac{R_p}{G}, \quad (8a)$$

$$a_2 = -\frac{R_m((R_{vca} + R'_s)R'_C + R_{vca}R'_s)R_p}{GN^2(R'_C + R'_s)}. \quad (8b)$$

The dynamic coupling between the 3 domains results from (2) and (3) and is given by the off-diagonal matrices

$$\mathbf{A}_{13} = \begin{bmatrix} \frac{Gk_m(R_m + R_p)}{R_p N m} & \frac{R_m k_m}{N m} \\ 0 & 0 \end{bmatrix}, \quad \mathbf{A}_{31} = \begin{bmatrix} -\frac{R_p k_m}{NG} & 0 \\ 0 & 0 \end{bmatrix}, \quad (9a)$$

$$\mathbf{A}_{23} = \begin{bmatrix} \frac{GR'_s R'_C (R_m + R_p)}{NR_p (R'_C + R'_s) L'} & \frac{R'_C R'_s R_m}{N (R'_C + R'_s) L'} \\ -\frac{GR'_s (R_m + R_p)}{C' N R_p (R'_C + R'_s)} & \frac{-R'_s R_m}{C' N (R'_C + R'_s)} \\ \frac{-GR'_C (R_m + R_p)}{NR_p (R'_C + R'_s) C'_s} & \frac{-R'_C R_m}{C'_s N (R'_C + R'_s)} \end{bmatrix}, \quad (9b)$$

$$\mathbf{A}_{32} = \begin{bmatrix} \frac{R'_s R'_C R_p}{NG (R'_C + R'_s)} & \frac{R'_s R_p}{NG (R'_C + R'_s)} & \frac{R'_C R_p}{NG (R'_C + R'_s)} \\ 0 & 0 & 0 \end{bmatrix}. \quad (9c)$$

### III. CONTROL DESIGN

#### A. Integrated state-control structure

Based on the system model (4) an optimal LQR state-space controller is now derived. Fig. 3 shows the proposed control structure, including the physical electro-mechanical system with its measured outputs  $x$  and  $i_{vca}$  and two first-order low-pass anti-aliasing filters ( $G_{LP,i}$ ,  $G_{LP,x}$ ). The LQR requires full-state feedback, but only two of the 7 system states are directly measured. For this reason a Kalman-filter (KF) is included as a state-observer.

The goal of the control is to track a reference position  $x^d$ , therefore the LQR is formulated in the translated coordinates

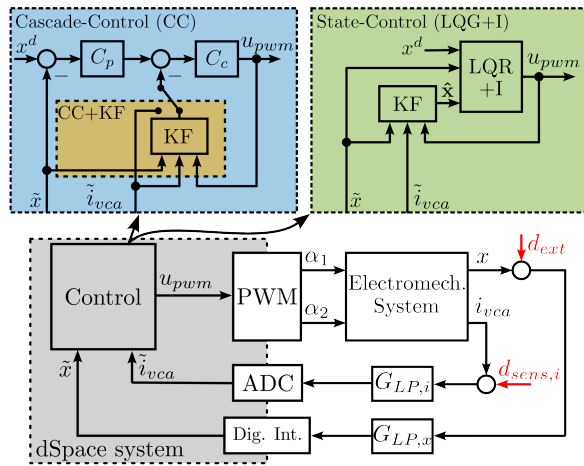


Fig. 3. Block diagram of proposed integrated control-structure and the cascade-control structure. The integrated control structure uses an LQR with integrator (LQR+I) state-space controller in combination with a Kalman-filter (KF) for the estimation of the unmeasured states (LQG+I). The cascade-controller consists of the inner current controller  $C_c$  and the position controller  $C_p$ . The current measurement can either be used directly (CC) or in combination with the KF (CC+KF).

$\mathbf{z} = \mathbf{x} - \mathbf{x}_S$  and  $u^* = u - u_S$ , with  $\mathbf{x}_S$  and  $u_S$  being the steady-state state-vector and control input respectively. Setting  $\mathbf{0} = \mathbf{A}\mathbf{x} + \mathbf{b}u$  with (4) and solving for each state and  $u$  depending on the desired position  $x^d$  yields

$$\mathbf{x}_S = \underbrace{\begin{bmatrix} 0 & 1 & \frac{k}{k_m} & \frac{R_{vca}k}{k_m} & \frac{R_{vca}k}{k_m} & 0 & \frac{Nk}{R_m k_m} \end{bmatrix}^T}_{\mathbf{x}} x^d, \quad (10a)$$

$$u_S = \underbrace{k}_{\tilde{U}} \frac{R_L + R_{vca}}{k_m} x^d. \quad (10b)$$

To cope with model uncertainties and slow changes in system parameters, like changing actuator resistance due to heating, an integrator is included in the LQR control design (LQR+I). The system model (4) is discretized with the sample time  $T_s$  and an integrator state  $z^I$  is included

$$\mathbf{z}^a = \begin{bmatrix} \mathbf{z} \\ z^I \end{bmatrix}, \quad z_{k+1}^I = z_k^I + T_s (x_k^d - \tilde{x}_k), \quad (11)$$

forming the augmented discrete time system

$$\mathbf{z}_{k+1}^a = \Phi^a \mathbf{z}_k^a + \Gamma^a u_k, \quad (12a)$$

$$y_k = \mathbf{C}^a \mathbf{z}_k^a. \quad (12b)$$

Taking (11) into account, the augmented state-space matrices result to

$$\Phi^a = \begin{bmatrix} \Phi & \mathbf{0} \\ -\mathbf{C}_1 & 0 \end{bmatrix}, \quad \Gamma^a = \begin{bmatrix} \Gamma \\ 0 \end{bmatrix}, \quad (13)$$

with  $\Phi$  and  $\Gamma$  denoting the discretized dynamic matrix and input vector of the system (4) and  $\mathbf{C}_1$  being the first row of the matrix  $\mathbf{C}$ . This is, because for the integral part only the measured position  $\tilde{x}$  is considered. With a positive semi-definite matrix  $\mathbf{Q} \in \mathbb{R}^{8 \times 8}$  and the positive constant  $R \in \mathbb{R}$ , the

LQR feedback gain  $\mathbf{K}$  is calculated with the Matlab command `lqr` by minimizing the cost function [24]

$$\arg \min_{u_k} J(u_k) = \sum_{k=1}^{\infty} (\mathbf{z}^T \mathbf{Q} \mathbf{z} + u_k^T \mathbf{R} u_k). \quad (14)$$

In the same manner the KF is designed with the command `kalmd` for the discrete system model without additional integrator state. It is parameterized with the (continuous) process-noise covariance matrix  $\mathbf{Q}_n \in \mathbb{R}^{7 \times 7}$  and the measurement noise covariance matrix  $\mathbf{R}_n \in \mathbb{R}^{2 \times 2}$  delivering the estimated system states  $\hat{\mathbf{x}}$  by

$$\hat{\mathbf{x}}_{k+1} = \Phi \hat{\mathbf{x}}_k + \Gamma u_k + \mathbf{L} (y_k - \mathbf{C} \hat{\mathbf{x}}_k), \quad (15)$$

with the KF gain matrix  $\mathbf{L} \in \mathbb{R}^{7 \times 2}$ . Given the state estimate from the KF and by using (10), the final control output of the state-control scheme is calculated via

$$u_k = \underbrace{\begin{bmatrix} \mathbf{K}_z & K_I \end{bmatrix}}_{\mathbf{K}} \begin{bmatrix} \hat{\mathbf{x}}_k - \mathbf{X} x_k^d \\ z_k^I \end{bmatrix} + U x_k^d. \quad (16)$$

The closed-loop stability of the linear plant controlled by an LQR is given by design and the stability of the combination of LQR and KF is given by the separation theorem for linear systems [24], [25].

### B. Cascade-control structure

As a reference control structure, a conventional cascade-control scheme is derived with a loop-shaping approach [5] in the frequency domain. As shown in Fig. 3, it consists of the outer position controller  $C_p$  and the inner current controller  $C_c$ . The current controller is comprised of a PI-controller  $C_{PI}$  and notch-filter  $C_n$  with the structure

$$C_{PI}(s) = \frac{k_{I,c}}{s} (1 + sT_I), \quad (17a)$$

$$C_n(s) = \frac{s^2 + 2D\xi\omega_n s + \omega_n^2}{s^2 + 2\xi\omega_n s + \omega_n^2}, \quad (17b)$$

according to  $C_c(s) = C_{PI}(s)C_n(s)$  in the Laplace domain. The notch-filter is tuned for suppressing the resonance peak of the LC-output filter of the switched amplifier (Fig. 2) and therefore enables a higher bandwidth of the current control loop.

The position controller is implemented as PID-controller with the structure [26]

$$C_p(s) = k_p + \frac{k_{I,p}}{s} + \frac{k_{d,s}}{1 + sT_t}. \quad (18)$$

Additionally to the direct measurement of the position and the current, the possibility of using the estimated current signal from the KF is added (yellow CC+KF block in Fig. 3).

### IV. POSITION UNCERTAINTY ANALYSIS

To analyze the impact of disturbances and noise sources on the position uncertainty of the system, dynamic error budgeting can be used [27]–[29]. Every error source in the system is modeled as an (equivalent) noise source with a certain power spectral density (PSD), and its contribution to the position uncertainty is calculated with the sensitivity function

$|S(j\omega)|^2$  from error location to the output  $x$  [30]. Therefore the frequency domain representation of the controller and the plant are required for the calculation.

### A. Frequency domain representation

As shown in Fig. 3, the derivation of the sensitivity functions in the case of cascade-control (CC) is straightforward, as the controllers are directly available as frequency domain transfer functions. Further the transfer functions from the voltage  $u$  to the actuator current  $i_{vca}$  and the position  $x$  can be derived from the introduced state-space model (4) via

$$\begin{bmatrix} G_{xu}(s) \\ G_{iu}(s) \end{bmatrix} = \mathbf{C}(s\mathbf{I} - \mathbf{A})^{-1} \mathbf{b}. \quad (19)$$

In the proposed state-control case however, the general block diagram in Fig. 3 does not intuitively lead to a frequency domain representation of the controller. It is thus redrawn as shown in Fig. 4. All control structures can be represented

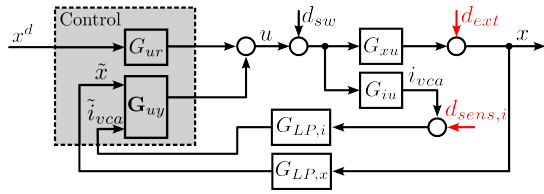


Fig. 4. System block-diagram used for dynamic error budgeting with frequency domain representation of the control. The modeled error sources affect the system at the locations represented with arrows.

in the frequency domain by the transfer function  $G_{ur}$  from the reference position  $x^d$  to the control output  $u$ , and the transfer matrix  $\mathbf{G}_{uy} \in \mathbb{R}^{1 \times 2}$  from the measurement to the control output. In the case of LQG+I they are derived by using (10), (11), (15), (16) and the superposition principle for linear systems. By z-transformation of (11) and (15),  $z^I$  and  $\hat{\mathbf{x}}$  can be expressed by

$$z^I = \frac{1}{z-1} (x^d - [1 \ 0] \mathbf{y}), \quad (20a)$$

$$\hat{\mathbf{x}} = \mathbf{\Lambda} \mathbf{L} \mathbf{y} + \mathbf{\Lambda} \mathbf{\Gamma} u, \quad (20b)$$

with  $\mathbf{\Lambda} = (z\mathbf{I} - \mathbf{\Phi} + \mathbf{L}\mathbf{C})^{-1}$ . Substituting (20a) into the z-transform of (16) yields

$$u = \mathbf{K}_z (\hat{\mathbf{x}} - \mathbf{X}x^d) + Ux^d + \frac{K_I}{z-1} (x^d - [1 \ 0] \mathbf{y}). \quad (21)$$

After including (20b) into (21) and solving for  $u$ , the frequency domain transfer function of the state-control structure (LQG+I) can be expressed by

$$u = \underbrace{(1 - \mathbf{K}_z \mathbf{\Lambda} \mathbf{\Gamma})^{-1} \left( \mathbf{K}_z \mathbf{\Lambda} \mathbf{L} - \frac{K_I}{z-1} [1 \ 0] \right)}_{\mathbf{G}_{uy} = \begin{bmatrix} G_{ux} \\ G_{ui} \end{bmatrix}} \underbrace{\begin{bmatrix} \hat{\mathbf{x}} \\ \mathbf{y} \end{bmatrix}}_{\mathbf{y}} + \underbrace{(1 - \mathbf{K}_z \mathbf{\Lambda} \mathbf{\Gamma})^{-1} \left( U + \frac{K_I}{z-1} - \mathbf{K}_z \mathbf{X} \right)}_{G_{ur}} x^d. \quad (22)$$

In the cascade-control case (CC) and in the case where the cascade-control is extended with the KF (CC+KF), the control system can also be expressed by  $G_{ur}$  and  $\mathbf{G}_{uy}$ . The derivation is done in a similar manner as in the demonstrated case of state-control.

### B. Position error sources

Several error sources affect the position accuracy of the system under investigation. They include external noise sources like power-supply noise or current measurement noise, non-linear effects of some system components, like PWM switching or quantization effects, or the discrete implementation of the controllers. For reasons of simplicity, only the most prominent position error sources are considered. In Fig. 3 and Fig. 4, the location of the error sources in the control-loop are shown.

The current sensor noise  $d_{noise}$  consists of the electrical noise introduced by the sensing shunt resistor and its corresponding current-sense amplifier. Based on measurements (data not shown), the current sensor noise can be approximated by a constant PSD  $n_{sens,i}$  ( $\text{A}^2/\text{Hz}$ ). Considering that the current is sampled with the switching frequency of the current amplifier  $T_s$ , this noise value has to be multiplied with some factor  $k_{alias}$ , to also account for aliased noise components with frequencies greater than the Nyquist frequency  $f_N = 1/2T_s$ . The cut-off frequency  $f_c$  of the 1st-order anti-aliasing filter ( $G_{LP,i}$  in Fig. 4) is chosen to not introduce significant delays in the feedback loop. For determining the factor  $k_{alias}$ , the concept of the equivalent noise-bandwidth  $f_{enb}$  is used, in which the frequency behaviour of  $G_{LP,i}$  is approximated by an ideal low-pass with unity gain up to the equivalent noise-bandwidth  $f_{enb}$ . For a 1st-order lowpass it can be shown, that for equivalent noise energy on the output this frequency is  $f_{enb} = \frac{\pi}{2} f_c$  [31], which leads to

$$k_{alias} = \frac{f_{enb}}{f_N} = \frac{\pi}{2} f_c 2T_s = \pi f_c T_s. \quad (23)$$

The current sensor noise used for dynamic error budgeting  $d_{sens,i}$  follows accordingly with  $d_{sens,i} = k_{alias} n_{sens,i}$ .

The external disturbance  $d_{ext}$  is dominated by vibrations of the environment which are transmitted to the mover via the flexure stiffness. It is determined by recording the position signal  $x$  with disabled controllers for several seconds and performing a Fast Fourier Transform (FFT) on the time-domain data. The worst-case over multiple measurements is taken for calculating the PSD.

It is important to point out, that the PWM switching results in voltage ripple at the output of the current amplifier  $d_{sw}$ , which exhibits its first harmonic at twice the switching frequency of the PWM full-bridge (see Fig. 1). Considering the incorporation of the LC-output filter and that the suspended mover acts as a 2nd-order mechanical low-pass, the impact on the position uncertainty is negligible. This point will be further reinforced in the next section through the analysis of the error sensitivity function.

### C. Error sensitivity functions

The error sensitivity functions represent the sensitivity of the position  $x$  to the respective error source ( $d_{sens,i}$ ,  $d_{ext}$ ,  $d_{sw}$ ). The derivation procedure is equivalent for all cases and is demonstrated for the current measurement noise  $d_{sens,i}$ :

- 1) Set  $x^d$ ,  $d_{sw}$  and  $d_{ext}$  to zero (superposition principle).
- 2) Calculate the plant transfer functions  $G_{xu}(s)$  and  $G_{iu}(s)$  (19) and the controller transfer matrix  $\mathbf{G}_{uy}$  (22).
- 3) Use the block-diagram (Fig. 4) and solve for  $x(s)$  depending on  $d_{sens,i}(s)$  in the frequency domain.
- 4) The error sensitivity function is then given by  $S_{sens,i}(s) = \frac{x(s)}{d_{sens,i}(s)}$

The resulting error sensitivity function is given by

$$S_{sens,i}(s) = \frac{G_{ui}G_{xu}G_{LP,i}}{1 - G_{ui}G_{iu}G_{LP,i} - G_{ux}G_{xu}G_{LP,x}}. \quad (24)$$

In Fig. 5 the error sensitivity functions are plotted together with the PSD of the investigated error sources  $d_{sens,i}$  and  $d_{ext}$ . The values for the system parameters and error sources are

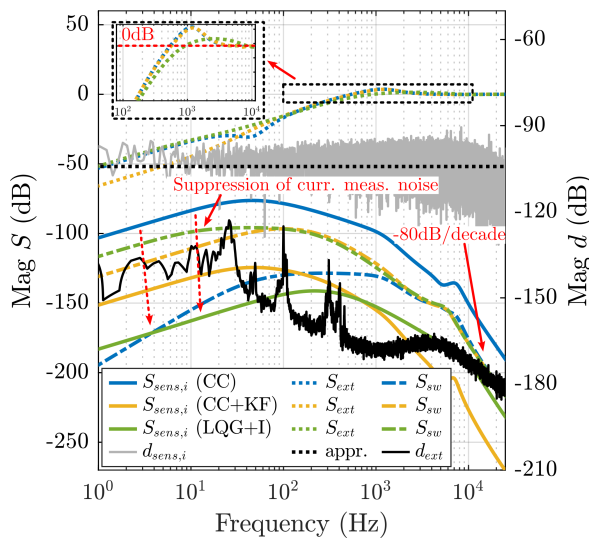


Fig. 5. Error sensitivity functions (colored, left y axis) and PSD of current measurement noise  $d_{sens,i}$  ( $A^2/Hz$ ) and external disturbances ( $m^2/Hz$ ) (gray/black, right y axis) for the CC, CC+KF and LQG+I case. The suppression of current measurement noise with the KF is highlighted by the dotted red arrows.

taken from the actual experimental prototype system, which is developed in Section V-A, and the controller parameter tuning is discussed in the next section. From the error sensitivity functions it is apparent, that the incorporation of the KF offers a significantly enhanced capability to attenuate the prevailing current measurement noise compared to the cascade-control case without KF (colored, solid lines). By adjusting the respective entry of the  $\mathbf{R}_n$ -matrix of the KF, it is possible to tune the current measurement noise sensitivity  $S_{sens,i}$ , thus allowing for adaption of the desired noise rejection performance.

Further it is evident, that the rejection of external disturbances is similar across all three investigated cases. This similarity arises from the tuning of the control schemes to the

TABLE I  
COST FUNCTION TERMS AND NORMALIZATION WEIGHTS

Cost function terms		Unit	Normalization weights	
$e_1$	$f_{3dB} - f_{3dB}^d$	Hz	$w_1$	10
$e_2$	$\max(0, x_{e,rms} - x_{e,rms}^{max})$	m	$w_2$	$1 \cdot 10^{-9}$
$e_3$	$\ T(s)\ _{\infty}$	dB	$w_3$	1
$e_4$	$\ S(s)\ _{\infty}$	dB	$w_4$	2
$e_5$	$ S(j2\pi 1 \text{ Hz}) $	1	$w_5$	$5 \cdot 10^{-3}$

same closed-loop bandwidth and the inclusion of an integrator in each case. Interestingly in the CC+KF case, the external disturbance rejection is even enhanced in the lower frequency range. Conversely, the LQG+I configuration shows superior disturbance rejection within the frequency range from 200 Hz to 2 kHz, as illustrated in the zoomed section of Fig. 5.

Additionally, the sensitivity to voltage ripple from PWM-switching is plotted (colored, dash-dotted lines), which shows a  $-80$  dB per decade slope after the cut-off frequency of the LC-output filter. This confirms that the position uncertainty contribution of the high frequent voltage ripple (100 kHz) for the prototype setup) is negligible.

### D. Controller parameter tuning

Based on the system model and presented error analysis in the frequency domain, the LQR+I controller and the KF are systematically tuned to a desired performance. Therefore the dynamic position error  $x_e$  is evaluated, by applying the sensitivity functions to the PSD of the error sources. The resulting output position error PSD originating from each error source can be calculated by [30]

$$|PSD_{x,sens,i}(f)| = |S_{sens,i}(s)|^2 |d_{sens,i}(f)|, \quad (25a)$$

$$|PSD_{x,ext}(f)| = |S_{ext}(s)|^2 |d_{ext}(f)|. \quad (25b)$$

For uncorrelated error sources, the total PSD of the position error is then given by [30]

$$|PSD_{x,tot}(f)| = |PSD_{x,sens,i}(f)| + |PSD_{x,ext}(f)|. \quad (26)$$

By now integrating over the relevant frequency range  $[f_1, f_2]$ , the rms-value of the position uncertainty in the time-domain is calculated by

$$x_{e,rms} = \sqrt{\int_{f_1}^{f_2} |PSD_{x,tot}(f)| df}. \quad (27)$$

With this formulation of the positioning uncertainty, together with the frequency domain representation of the controller and the plant, the control objectives can be expressed in a cost function depending on the controller parameters. This allows the formulation of the control parameter tuning process as a multi-dimensional optimization problem

$$\min_{\mathbf{Q}_n, \mathbf{R}_n, \mathbf{Q}, R} J(\mathbf{Q}_n, \mathbf{R}_n, \mathbf{Q}, R) = \sum_{k=1}^5 \left( \frac{e_k}{w_k} \right)^2, \quad (28)$$

with several cost terms  $e_k$  and normalization weights  $w_k$ , which are summarized in Table I. In addition to (27), the calculation of the complementary sensitivity function  $T(s) = \frac{x(s)}{x^d(s)}$  and the sensitivity function  $S(s) = \frac{x(s)}{d_{ext}(s)}$  from Fig. 4 is required

for the evaluation of the cost function. It is to note that the dependency of the cost terms on the tuning parameters is not explicitly stated in the table for easier notation.

The principle goal of the control is to achieve a certain closed-loop bandwidth  $f_{3dB}^d$  in combination with a desired maximum positioning uncertainty  $x_{e,rms}^{max}$ . This is reflected in the cost function by penalizing the difference of  $f_{3dB}$  from the complementary sensitivity function  $T(s)$  to  $f_{3dB}^d$  and values  $x_{e,rms}$  above  $x_{e,rms}^{max}$ . Secondly, to have good transient behavior and to maximize robustness, the  $H_\infty$ -norms of  $T(s)$  and  $S(s)$ , which correspond to the respective peak values in the magnitude functions, are penalized. Additionally to ensure sufficient rejection of low-frequent disturbances and model uncertainties, the absolute value of the sensitivity function  $S(s)$  evaluated at a frequency of 1 Hz is used. This term ensures that the introduced integrator in the control is tuned accordingly.

The cost function (28) is now minimized by varying the LQR+I and KF controller parameters  $\mathbf{Q}_n$ ,  $\mathbf{R}_n$ ,  $\mathbf{Q}$ , and  $\mathbf{R}$ . Since the number of tunable parameters is 118 in this case (refer to Section III-A), the matrices are chosen as diagonal matrices

$$\begin{aligned} \mathbf{Q}_n &= \text{diag}(\mathbf{q}_n), & \mathbf{q}_n &\in \mathbb{R}^7 \\ \mathbf{R}_n &= \text{diag}(\mathbf{r}_n), & \mathbf{r}_n &\in \mathbb{R}^2 \\ \mathbf{Q} &= \text{diag}(\mathbf{q}), & \mathbf{q} &\in \mathbb{R}^8 \\ \mathbf{R} & & &\in \mathbb{R}, \end{aligned} \quad (29)$$

which reduces the optimization problem to

$$\min_{\mathbf{q}_n, \mathbf{r}_n, \mathbf{q}, \mathbf{R}} J(\mathbf{Q}_n, \mathbf{R}_n, \mathbf{Q}, \mathbf{R}) = \sum_{k=1}^5 \left( \frac{e_k}{w_k} \right)^2, \quad (30)$$

with 18 tunable parameters. The optimization problem is solved with an interior-point algorithm of the *fmincon* command in Matlab. The starting parameter set for the algorithm is manually chosen considering known system properties. For example the entries for the measurement noise covariance matrix  $\mathbf{R}_n$  are chosen in dependence of the reliability of the respective measurement. Further, the entries in  $\mathbf{Q}$  corresponding to the position  $x$  and the integrated position error (state 2 and 8 of (12)) are weighted higher than the other entries.

## V. EXPERIMENTAL VALIDATION

To validate the derived system model and to evaluate the control structures with the optimized control parameters, an experimental prototype system of a 1 DoF precision positioning system is developed according to Section II-A. For this system, the theoretical dynamic error budget is evaluated with the derived sensitivity functions and compared to measurement data. Afterwards the dynamic behavior of the integrated control structure is experimentally compared against the cascade-controllers in the time-domain.

### A. Experimental prototype system

The manufactured prototype system of the high-precision 1 DoF positioning system is shown in Fig. 6. It employs the lightweight mover held in place by an aluminium flexure structure and the VCA (VCAR0087-0062-00A, Supt Motion,

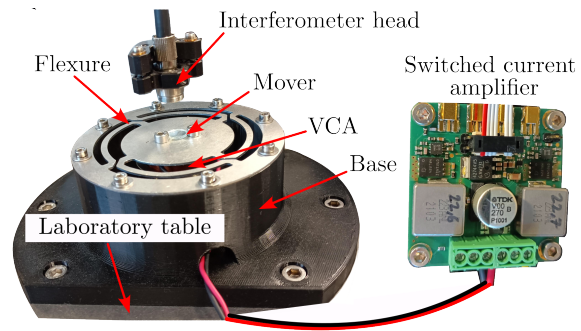


Fig. 6. High-precision 1 DoF positioning system with Lorentz-type positioning mechanism, optical interferometer position measurement, and custom-made switched current amplifier.

CN) serving as the positioning mechanism. On top of the mover a reflective mirror is mounted, enabling sub-nm position measurement with an interferometer (IDS3010, AttoCube Systems AG, Germany). The 3D-printed base holding the flexure and the stator part of the VCA is mounted on a vibration isolated laboratory table. On the right of Fig. 6 the custom-made switched current amplifier (see Fig. 1) connected to the VCA is shown. It has a maximum supply voltage of 24 V and an output current capability of up to 8 A. The controllers are implemented in a rapid prototyping system (MicroLabBox, dSPACE GmbH, Germany) with a sample-time of  $T_s = 1/50$  kHz.

To identify the model parameters of the built system, the measured frequency domain transfer function from the amplifier output voltage  $u_{pwm}$  to the actuator coil current  $i_{act}$  is shown in Fig. 7. The parameters corresponding to the derived

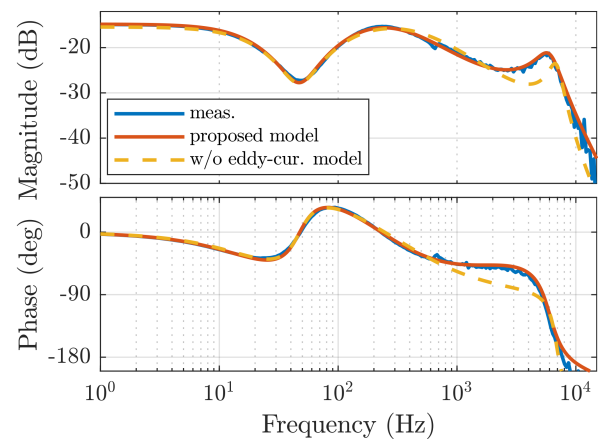


Fig. 7. Measured transfer function from  $u_{pwm}$  to  $i_{act}$  (blue). The parameter of the system model (4) are derived by solving a non-linear least-squares curve fitting problem (red). Without the eddy-current model in Fig. 2 (constant inductance of VCA) the fitted model deviates from the measurement at higher frequencies (yellow).

system model Fig. 2 are then determined by numerically solving a non-linear least-squares curve fitting problem to the measured response with Matlab. The resulting model transfer

TABLE II  
SYSTEM AND CONTROL PARAMETERS

$L_1$	22.5 $\mu$ H	$R_p$	1·10 <sup>8</sup> 1/H
$R_{L1}$	70 m $\Omega$	$R_m$	3.47·10 <sup>7</sup> 1/H
$C_1$	15 $\mu$ F	$k_m$	12.87 N/A
$R_{C1}$	10 m $\Omega$	$m$	47·10 <sup>-3</sup> kg
$C_{s1}$	21 $\mu$ F	$k$	4.1·10 <sup>3</sup> N/m
$R_{s1}$	1.35 $\Omega$	$d$	8.79 N s/m
$R_{vca}$	5.36 $\Omega$	$T_s$	1/50 kHz
$G$	1.98·10 <sup>3</sup> 1/ $\Omega$	$n_{sens,i}$	6·10 <sup>-12</sup> A <sup>2</sup> /Hz
$N$	243	$f_c$	100 kHz
$V_s$	16 V		
Cascade-control (CC)			
$k_{I,c}$	1.08·10 <sup>-4</sup>	$T_I$	1.08·10 <sup>-4</sup>
$\omega_n$	33.6·10 <sup>3</sup>	$D$	0.398
$\xi$	0.4	$k_p$	5.57·10 <sup>3</sup>
$k_{I,p}$	7.78·10 <sup>5</sup>	$k_d$	8.87
$T_t$	7.86·10 <sup>-5</sup>		
State-control (LQG+I)			
$\mathbf{q}$	[2.6·10 <sup>8</sup> 4.6·10 <sup>15</sup> 0.78 0.17 0.08 0.003 0.44 2.4·10 <sup>19</sup> ]		
$R$	1		
$\mathbf{q}_n$	[1.62·10 <sup>7</sup> 1.95·10 <sup>9</sup> 2.5 1.35 1.77 0.97 1.75] · 10 <sup>-6</sup>		
$\mathbf{r}_n$	[2.3·10 <sup>-12</sup> 0.57]		

function is represented by the red curve in Fig. 7. It is to mention that electrical component values which are easily accessible to measurement are fixed to their measured value to reduce the number of unknown parameters for the curve fitting problem. To evaluate the influence of the proposed eddy-current model on the modeling accuracy, additionally to the presented model a simplified model is derived which assumes a constant VCA inductance instead of the magnetical model part in Fig. 2. The result of the numerical curve fitting result for the simplified model is shown with the yellow line in Fig. 7. Both models match the measurement very well in the lower frequency range, whereas the simple model starts deviating from the measured response at higher frequencies, at which eddy-current effects start to emerge. The identified system parameters for the full model are summarized in Table II.

To enable a fair comparison between the control structures, both the state-controller and frequency domain controllers are tuned for the same closed-loop positioning bandwidth of  $f_{3dB}^d = 700$  Hz. The current loop of the cascade-control structure is tuned to be a factor 5 faster than the outer position loop. Measurements on the experimental system reveal a phase-margin of 50 deg for the cascade-controller (data not shown).

For the tuning of the LQG+I control a positioning uncertainty of 1 nm (rms) is targeted, so  $x_{e,rms}^{max}$  is set to this value for the optimization (Section IV-D). It is to note, that single tuned parameters largely vary for different starting parameter sets used in the optimization, as the defined error function (30) is not equally sensitive to all tunable parameters. However, this variation had no visible impact on the measurement results presented in this section. Additionally, Monte-Carlo simulations with the optimized parameter set are performed with variations up to 15% of the nominal plant parameters, which covers typical component variations in reality (data not shown). In all cases, the closed-loop system remains stable, giving an indication of the control systems robustness. The optimized LQG+I parameters and the parameters of the cascade-

controller are given in Table II in the continuous domain and are transformed to their respective discrete counterpart for the implementation on the experimental setup.

## B. Evaluation of dynamic error budget

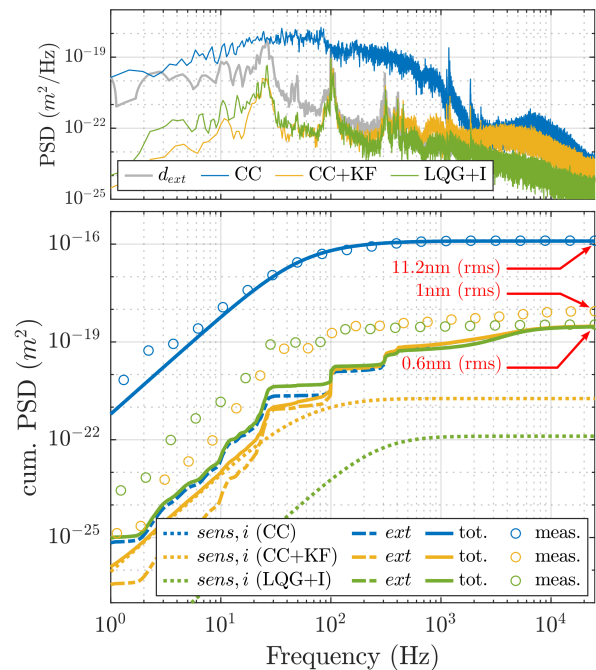


Fig. 8. Measured PSD of steady-state position error and PSD of external disturbances  $d_{ext}$  ( $m^2/Hz$ ) (top plot). Evaluation of the dynamic error budget: Theoretical and measured cumulative PSD of position error ( $m^2$ ) plus division into respective error source. The corresponding rms position uncertainty for a normal distribution is marked for the end-values of the experimental data (bottom plot).

In this section the dynamic error budget for each control structure is evaluated and compared to experimental data. The results are shown in Fig. 8, in which the measured PSD of steady-state position error and the cumulative PSD for each control-scheme is plotted, together with its division into the contribution from current measurement noise ( $d_{sens,i}$ ) and external disturbances ( $d_{ext}$ ). As expected from the sensitivity analysis in Fig. 5 the dominating error source for classical cascade-control (CC) is the current measurement noise, whereas for the other cases with included KF (CC+KF, LQG+I) external disturbances are dominating. With a position uncertainty of 0.6 nm and 1 nm (rms), LQG+I and CC+KF show more than a tenfold improvement as compared to the 11.2 nm (rms) in the case without KF (CC). The circles in the plot represent the calculated cumulative PSD from measured time-domain data on the prototype setup, which match the theoretical values from the dynamic error budget evaluation very well. The results show, that the first control objective of a positioning uncertainty below 1 nm (rms) is clearly achieved by the optimization based controller parameter tuning from Section IV-D.

### C. System dynamics evaluation

In addition to the dynamic error budgeting analysis, the control-structures are evaluated with respect to closed-loop system dynamics and position uncertainty in the time-domain on the prototype setup. Fig. 9 shows the measured position  $\hat{x}$  and the corresponding control output  $u_{vca}$  for multiple steps on the reference input. All control-schemes exhibit a similar

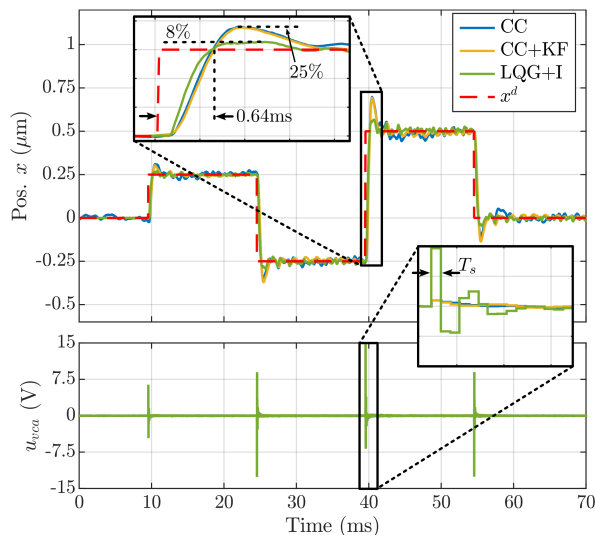


Fig. 9. Comparison of cascade-control (CC), cascade-control with Kalman-filter (CC+KF) and full-state control (LQG+I) for a steps on the reference input  $x^d$ . On the bottom the control action  $u_{pwm}$  is plotted for all three cases.

rise-time of 0.64 ms, as they are tuned for the same closed-loop bandwidth. The frequency domain controllers show an overshoot of 25%. In the dynamic comparison the integrated state-control structure is clearly superior over the other control schemes with 8% overshoot, which corresponds to an improvement of 17%. The slight oscillations after the step result from the excitation of structural modes of the mechanical system, which emerge a few hundred Hertz beyond the closed-loop bandwidth of the controllers. These modes are excited due to the step-function as reference input, which could be avoided with smoother motion profiles, e.g. minimum-jerk trajectories [6].

The precision and steady-state position uncertainty is evaluated in Fig. 10, in which the system response to multiple 5 nm steps at the reference input is shown. Additionally, the normalized empirical probability density function (EPDF) of the position signal in the grey shaded steady-state area is plotted together with a Gaussian fit on the right side. It confirms that the steady-state position uncertainty closely fits a normal distribution and that the values from the dynamic error budget analysis in the frequency domain match the time-domain data (refer to Fig. 8).

In summary, the effectiveness of the proposed tuning procedure for the integrated state-control (LQG+I) is successfully demonstrated on the experimental setup, achieving subnanometer positioning uncertainty and superior dynamic po-

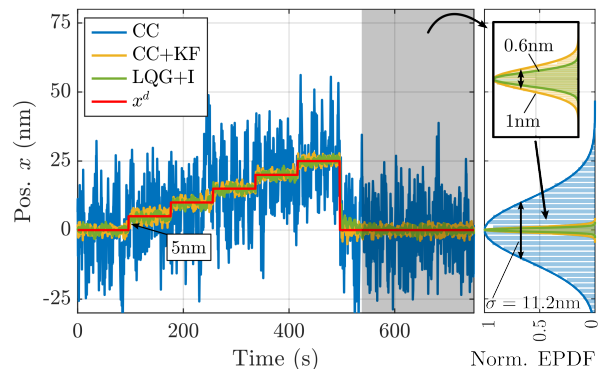


Fig. 10. Comparison of cascade-control (CC), control-control with Kalman-filter (CC+KF) and full-state control (LQG+I) for 5nm steps on the reference input  $x^d$  (left). Normalized Empirical Probability Density Function (EPDF) of the steady-state position and Gaussian fit (right).

sition tracking performance compared to the cascade-control structures (CC, CC+KF).

## VI. CONCLUSION

This paper presents the integrated mechatronic and control design of a switched amplifier-driven high-precision positioning system. In addition to classical cascade-controllers (CC, CC+KF) a highly integrated state-control structure (LQG+I) is designed based on a comprehensive mathematical system model considering the mechanical, electrical and magnetical system. An optimization based tuning process is proposed for the parameters of the LQR+I controller and KF, considering both dynamic requirements and a targeted steady-state positioning uncertainty, which is enabled by a dynamic error budget analysis in the frequency domain. The analysis reveals a steady-state positioning uncertainty of 0.6 nm (rms) for the tuned state-control structure (LQG+I), which is more than a tenfold improvement compared to a classical cascade-control structure (11.2 nm). Experimental measurements on a built prototype system confirm these results and further demonstrate fast reference position tracking with a rise-time of 0.64 ms in a step-response. While the achieved positioning uncertainties of the cascade-controller with included KF (CC+KF) and LQG+I are comparable, LQG+I exhibits superior dynamic tracking performance, featuring 17% less overshoot in a step-response.

## REFERENCES

- [1] H. Butler, "Position control in lithographic equipment [applications of control]," *IEEE Control Systems*, vol. 31, no. 5, pp. 28–47, 2011.
- [2] G. Schitter, K. J. Astrom, B. E. DeMartini, P. J. Turner, K. L. Turner, and P. K. Hansma, "Design and modeling of a high-speed AFM-scanner," *IEEE Transactions on Control Systems Technology*, vol. 15, no. 5, pp. 906–915, 2007.
- [3] L. Jonušauskas, D. Gailevičius, S. Rekštytė, T. Baldacchini, S. Juodkazis, and M. Malinauskas, "Mesoscale laser 3d printing," *Optics Express*, vol. 27, no. 11, p. 15205, 2019.
- [4] N. H. Vrijsen, J. W. Jansen, and E. A. Lomonova, "Comparison of linear voice coil and reluctance actuators for high-precision applications," in *Proceedings of 14th International Power Electronics and Motion Control Conference EPE-PEMC 2010*. IEEE, 2010.
- [5] R. M. Schmidt, G. Schitter, and A. Rankers, *The design of high performance mechatronics: High-tech functionality by multidisciplinary system integration*. Ios Press, 2020.

- [6] S. Ito, J. Steininger, and G. Schitter, "Low-stiffness dual stage actuator for long range positioning with nanometer resolution," *Mechatronics*, vol. 29, pp. 46–56, 2015.
- [7] D. Wertjanž, E. Csencsics, and G. Schitter, "Three-DoF vibration compensation platform for robot-based precision inline measurements on free-form surfaces," *IEEE Transactions on Industrial Electronics*, vol. 69, no. 1, pp. 613–621, 2022.
- [8] H. Shinno, H. Yoshioka, and H. Sawano, "A newly developed long range positioning table system with a sub-nanometer resolution," *CIRP Annals*, vol. 60, no. 1, pp. 403–406, 2011.
- [9] T. J. Teo, G. Yang, and I.-M. Chen, "A flexure-based electromagnetic nanopositioning actuator with predictable and re-configurable open-loop positioning resolution," *Precision Engineering*, vol. 40, pp. 249–260, 2015.
- [10] S. Ito and G. Schitter, "Comparison and classification of high-precision actuators based on stiffness influencing vibration isolation," *IEEE/ASME Transactions on Mechatronics*, vol. 21, no. 2, pp. 1169–1178, 2016.
- [11] S. Ito, S. Pirker, and G. Schitter, "Integrating PWM amplifier with the design of mechatronic systems for energy-efficient precision motion," *IEEE Journal of Industry Applications*, vol. 10, no. 2, pp. 134–141, 2021.
- [12] M. Mauerer, A. Tuysuz, and J. W. Kolar, "Low-noise isolated digital shunt for precision class-d power amplifiers," *IEEE Transactions on Power Electronics*, vol. 33, no. 3, pp. 1907–1910, 2018.
- [13] P. Sriyotha, K. Nakamoto, M. Sugai, and K. Yamazaki, "Development of 5-axis linear motor driven super-precision machine," *CIRP Annals*, vol. 55, no. 1, pp. 381–384, 2006.
- [14] F. A. Qureshi, V. Spinu, K. Wijnands, and M. Lazar, "A real-time control system architecture for industrial power amplifiers," in *2013 American Control Conference*. IEEE, 2013.
- [15] S. J. Settels, J. van Duivenbode, and J. L. Duarte, "Impact of amplifier errors on position loop accuracy of high-precision moving stages," in *2017 19th European Conference on Power Electronics and Applications (EPE'17 ECCE Europe)*. IEEE, 2017.
- [16] M. Hajiheidari, D. Xu, J. van Duivenbode, B. Vermulst, and M. Lazar, "Analysis of power amplifier contribution to the precision of motion systems," in *2022 IEEE 17th International Conference on Advanced Motion Control (AMC)*. IEEE, 2022.
- [17] T. Riel, R. Saathof, A. Katalenic, and G. Schitter, "Noise analysis and improvement of a permanent magnet synchronous motor by dynamic error budgeting," *IFAC-PapersOnLine*, vol. 49, no. 21, pp. 339–346, 2016.
- [18] A. G. Gelen and A. Atasoy, "A new method for kalman filter tuning," in *2018 International Conference on Artificial Intelligence and Data Processing (IDAP)*. IEEE, 2018.
- [19] Z. Chen, C. Heckman, S. Julier, and N. Ahmed, "Weak in the nees?: Auto-tuning kalman filters with bayesian optimization," in *2018 21st International Conference on Information Fusion (FUSION)*. IEEE, 2018.
- [20] B. M. Åkesson, J. B. Jørgensen, N. K. Poulsen, and S. B. Jørgensen, "A generalized autocovariance least-squares method for kalman filter tuning," *Journal of Process Control*, vol. 18, no. 7–8, pp. 769–779, 2008.
- [21] N. Mohan, T. M. Undeland, and W. P. Robbins, *Power electronics: converters, applications, and design*. John Wiley & sons, 2003.
- [22] A. Brown, J. Ross, and K. Nichols, "Time-domain simulation of mixed nonlinear magnetic and electronic systems," *IEEE Transactions on Magnetics*, vol. 37, no. 1, pp. 522–532, 2001.
- [23] F. Baronti, A. Lazzeri, F. Lenzi, R. Roncella, R. Saletti, and S. Saponara, "Voice coil actuators: From model and simulation to automotive application," in *2009 35th Annual Conference of IEEE Industrial Electronics*, pp. 1805–1810, 2009.
- [24] S. Skogestad, *Multivariable feedback control*. John Wiley, 2005.
- [25] N. Lehtomaki, N. Sandell, and M. Athans, "Robustness results in linear-quadratic gaussian based multivariable control designs," *IEEE Transactions on Automatic Control*, vol. 26, no. 1, pp. 75–93, 1981.
- [26] E. Csencsics and G. Schitter, "Parametric PID controller tuning for a fast steering mirror," in *2017 IEEE Conference on Control Technology and Applications (CCTA)*. IEEE, 2017.
- [27] L. Jabben and J. Van Eijk, "Performance analysis and design of mechatronic systems," *Mikroniek*, vol. 51, no. 2, pp. 5–12, 2011.
- [28] A. Okyay, K. Erkorkmaz, and M. B. Khamesee, "Mechatronic design, actuator optimization, and control of a long stroke linear nanopositioner," *Precision Engineering*, vol. 52, pp. 308–322, 2018.
- [29] T. Riel, R. Saathof, A. Katalenic, S. Ito, and G. Schitter, "Noise analysis and efficiency improvement of a pulse-width modulated permanent

magnet synchronous motor by dynamic error budgeting," *Mechatronics*, vol. 50, pp. 225–233, 2018.

- [30] W. A. Gardner, *Introduction to random processes*. McGraw-Hill, 1989.
- [31] Texas Instruments, "Noise analysis in operational amplifier circuits," 2007. [Online]. Available: <https://www.google.at/>



**Daniel Pechgraber** is doctoral researcher in the Advanced Mechatronic Systems group at the Automation and Control Institute (ACIN) of TU Wien, Austria. He received an MSc. degree in Electrical Engineering from TU Wien in 2022. His primary research interests are on high-performance mechatronic systems design, high-precision motion control of linear and non-linear systems, as well as power electronics design for precision motion systems.



**Johannes Wiesböck** is doctoral researcher in the Advanced Mechatronic Systems group at the Automation and Control Institute (ACIN) of TU Wien, Austria. He received an MSc. degree in Electrical Engineering from TU Wien in 2021. His primary research interests are on design and system integration of high-precision opto-mechatronic measurement systems and optical sensing technologies for material analysis.



**Ernst Csencsics** is assistant professor for Metrology Systems in the Advanced Mechatronic Systems group at the Automation and Control Institute (ACIN) of TU Wien. He received an MSc and a PhD degree (sub auspiciis) in Electrical Engineering from TU Vienna, Austria in 2014 and 2017, respectively. His primary research interests are on high performance mechatronic systems, the development of holistic methods for multidisciplinary system design and integration, opto-mechatronic measurement and imaging systems, precision engineering, and robot-based in-line measurement systems. He received the journal best paper award of IEEE/ASME Transactions on Mechatronics (2018) and the best student paper award at the American Control Conference (2016).



**Georg Schitter** is Professor for Advanced Mechatronic Systems at the Automation and Control Institute (ACIN) of TU Wien. He received an MSc in Electrical Engineering from TU Graz, Austria (2000) and an MSc and PhD degree from ETH Zurich, Switzerland (2004). His primary research interests are on high-performance mechatronic systems, particularly for applications in the high-tech industry, scientific instrumentation, and mechatronic imaging systems, such as AFM, scanning laser and LIDAR systems, telescope systems, adaptive optics, and lithography systems for semiconductor industry. He received the journal best paper award of IEEE/ASME Transactions on Mechatronics (2018), of the IFAC Mechatronics (2008-2010), of the Asian Journal of Control (2004-2005), and the 2013 IFAC Mechatronics Young Researcher Award. He served as an Associate Editor for IFAC Mechatronics, Control Engineering Practice, and for the IEEE Transactions on Mechatronics.